Linear-time algorithm for phase-sensitive holography

Peter J. Christopher,* Ralf Mouthaan, Miguel El Guendy, and Timothy D. Wilkinson
University of Cambridge, Centre of Molecular Materials, Photonics and Electronics, Cambridge, England, United Kingdom

Abstract. Holographic search algorithms such as direct search (DS) and simulated annealing allow high-quality holograms to be generated at the expense of long execution times. This is due to single iteration computational costs of $O(N_xN_y)$ and number of required iterations of order $O(N_xN_y)$, where N_x and N_y are the image dimensions. This gives a combined performance of order $O(N_x^2N_y^2)$. We use a technique to reduce the iteration cost down to $O(1)$ for phase-sensitive computer-generated holograms, giving a final algorithmic performance of $O(N_xN_y)$. We do this by reformulating the mean-squared error (MSE) metric to allow it to be calculated from the diffraction field rather than requiring a forward transform step. For a 1024×1024-pixel test images, this gave us a ≈50,000× speed-up when compared with traditional DS with little additional complexity. When applied to phase-modulating or amplitude-modulating devices, the proposed algorithm converges on a global minimum MSE in $O(N_xN_y)$ time. By comparison, most extant algorithms do not guarantee that a global minimum is obtained. Those that do, have a computational complexity of at least $O(N_x^2N_y^2)$ with the naive algorithm being $O[(N_xN_y)!]$.
 [DOI: 10.1117/1.OE.59.8.085104]

Keywords: computer-generated holography; holographic predictive search; direct search; simulated annealing; linear time.

Paper 20200794 received Jul. 6, 2020; accepted for publication Aug. 13, 2020; published online Aug. 28, 2020.

1 Introduction

Holographic technology has developed significantly since its invention in 1948 by Dennis Gabor.[1] Conventional holography, developed since then, captures the interference pattern between a coherent light source and the light scattered off an object onto a photographic plate.[2] A three-dimensional (3-D) image of the object is then reconstructed when the photographic plate is exposed to a coherent light source.

The 1980s saw a breakthrough in holographic technology with the introduction of computer-generated holography. Improvements in computer processing power and the availability of computer-controlled spatial light modulators (SLMs) gave users more flexible approaches to modulate the spatial profile of an incident beam. In other words, the SLM enabled the flexible configuration of a hologram, something not possible using photographic plates. Advancements in this technology has revolutionized the display industry with it being applied in virtual reality and augmented reality systems.[3–5] In turn, positively influencing the wider information and education industries[6,7] as well as healthcare[8] and manufacturing,[9] holographic technology has also been used in lithography[10] and optical tweezing.[11]

In modern two-dimensional (2-D) holography systems, an SLM is used to modulate the profile of a coherent light beam. In the simplest configuration, an SLM is placed at the back focal plane of a lens with the aim of creating a desired light field at the front focal plane of the lens, as shown in Fig. 1. The back focal plane is termed the "diffraction field" H and the front focal plane is known as the "replay field" R, with the light fields in the two planes related by a Fourier transform $\mathcal{F}$ such that $R = \mathcal{F}\{H\}$. The aforementioned holograms are known as "Fraunhofer holograms," and it is possible to project light fields onto planes offset from the front focal planes, which are then known as "Fresnel holograms."

*Address all correspondence to Peter J. Christopher, E-mail: pjc209@cam.ac.uk

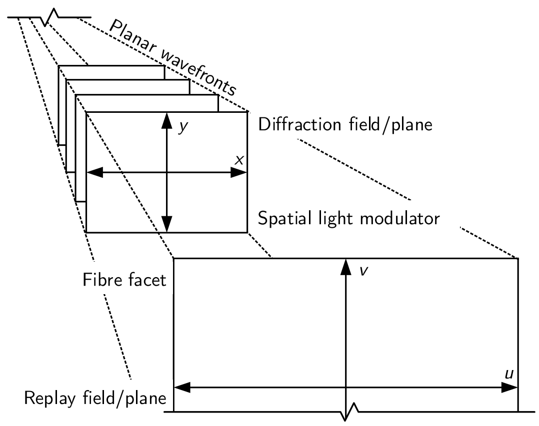

Fig. 1 Coordinate systems used in this work.

An SLM is a pixelated device, and as such it is intuitive to represent the diffraction field as discrete pixels. Similarly, the replay field can be represented by discrete pixels and the Fraunhofer transform relationship between the two planes can then be represented by two discrete Fourier transform relationships where the diffraction field coordinates are represented by x and y, and the replay field coordinates are represented by u and v. The N_x and N_y denote the size of the diffraction and replay fields along the horizontal and vertical axes, respectively. This expression assumes that the SLM is illuminated with a plane wave of uniform intensity and that the pixels have a fill factor of 100%.

$$R_{u,v} = \frac{1}{\sqrt{N_x N_y}} \sum_{x=0}^{N_x-1} \sum_{y=0}^{N_y-1} H_{x,y} e^{-2\pi i\left(\frac{ux}{N_x}+\frac{vy}{N_y}\right)}, \tag{1}$$

$$H_{x,y} = \frac{1}{\sqrt{N_x N_y}} \sum_{u=0}^{N_x-1} \sum_{v=0}^{N_y-1} R_{u,v} e^{2\pi i\left(\frac{ux}{N_x}+\frac{vy}{N_y}\right)}. \tag{2}$$

SLMs allow either the phase or amplitude of the incident light to be modulated but not both.[12] In addition, it is often the case that SLMs are digital devices and that only discrete modulation levels can be used. Projecting the desired replay field, known as the "target field" T, then corresponds to finding a diffraction field subject to these constraints that minimizes some error metric.[13] In this case, the phase-sensitive mean-squared error (MSE) shall be used.

$$\mathrm{Error}(T,R) = \frac{1}{N_x N_y} \sum_{u=0}^{N_x-1} \sum_{v=0}^{N_y-1} |T_{u,v} - R_{u,v}|^2. \tag{3}$$

The task of finding a computer-generated hologram becomes equivalent to minimizing this error metric. A variety of techniques has been developed to address this and one family of algorithms is briefly described in Sec. 2. These algorithms require repeated Fourier transforms, the evaluation of which is computationally expensive. This paper lays out an alternative approach to generating complex-valued (i.e., phase-sensitive) light fields that only requires a single transform to be used, after which the hologram can be determined using computationally inexpensive update steps. The fundamentals of this approach are laid out in Sec. 3.1 and are incorporated into a search algorithm in Sec. 3.2. Section 3.3 discusses how this approach lends itself to massive parallelization. Next, more realistic scenarios are considered, with conclusions being drawn for commercially available SLMs in Sec. 3.4 and Fresnel holograms being considered in Sec. 3.5. The algorithm is modified to account for a region of interest (RoI) in Sec. 4, which allows a much higher fidelity replay field to be projected. The approach described requires several orders of magnitude less computing power, but still yields replay fields of the highest quality.

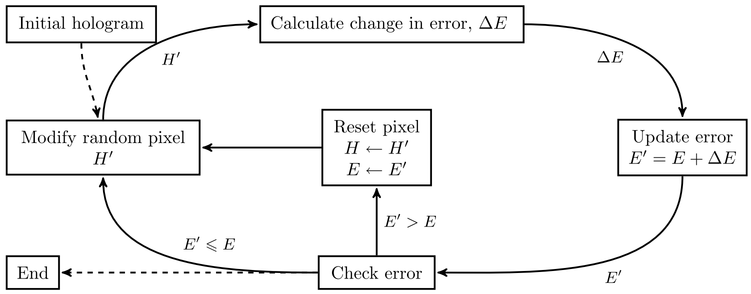

Fig. 2 The DS algorithm.

2 Established Holographic Search Algorithms

A widely used family of algorithms for phase-sensitive replay fields are the holographic search algorithms (HSAs), of which the most famous is perhaps direct search (DS).[14–19] Broadly speaking, these algorithms proceed by changing a pixel value and evaluating whether the error metric has improved. If the error metric has improved, the pixel change is adopted, else the pixel change is rejected. This process is illustrated in Fig. 2.

A second algorithm in this family is simulated annealing (SA),[20–24] which sometimes adopts pixel changes that do not improve the error metric in an effort to avoid local minima. HSAs are guaranteed to converge, but can converge extremely slowly and often to local rather than global minimum. Millions of iterations can be required before these algorithms have fully converged. This can be prohibitive if a full FFT is required at each iteration {complexity $O[N_x N_y \log(N_x N_y)]$}. Alternatively, evaluation of the full FFT can be avoided by using an update step that exploits the fact that only a single pixel is updated at a time. This gives an update step with complexity proportional to $O(N_x N_y)$, which is a marked improvement but can still give long run times for even medium-sized images as the complete algorithm will still run in $O(N_x^2 N_y^2)$. The authors have recently introduced several new HSAs that exploit geometric arguments to obtain significantly faster convergence,[25–28] but these, too, can still be computationally expensive to run.

3 Search in Linear Time

3.1 *Basic Premise*

For our initial investigation, we shall show that using known properties of the Fourier transform we can significantly reduce the computation required for generating phase-sensitive holograms. Note that we are only considering Fraunhofer holograms without a RoI, that is, the entire replay field is to be optimized. We shall extend our analysis to Fresnel holograms and refine our analysis to include an RoI later in this paper.

The Fourier transform operation obeys Parseval's theorem, reproduced in Eq. (4), where $A = \mathcal{F}(a)$, $B = \mathcal{F}(b)$, and an overline represents the complex conjugate. Parseval's theorem corresponds to energy conservation between the diffraction and replay field planes, which is the reason behind the $1/\sqrt{N_x N_y}$ term in Eqs. (1) and (2).

$$\sum_{x=0}^{N_x-1} \sum_{y=0}^{N_y-1} a_{x,y} \overline{b_{x,y}} = \sum_{u=0}^{N_x-1} \sum_{v=0}^{N_y-1} A_{u,v} \overline{B_{u,v}}. \tag{4}$$

The relationship between $H_{x,y}$ and $R_{u,v}$ has previously been defined as a Fourier transform. Similarly, a new field $G_{x,y}$ is defined, which corresponds to the inverse Fourier transform added to the "inverse" of the $T_{u,v}$. In effect, $G_{x,y}$ represents the diffraction field counterpart of the target replay field.

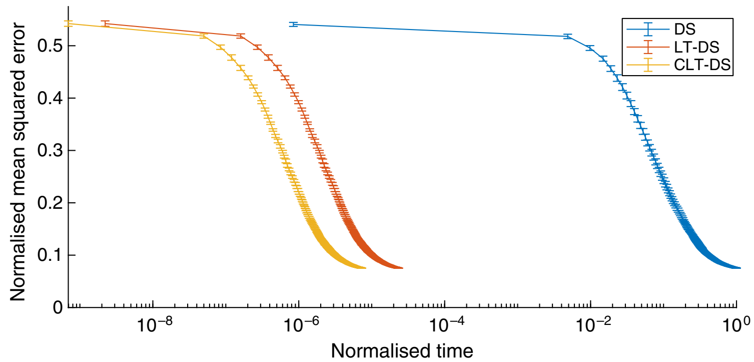

Fig. 3 Performance of DS and linear-time DS for a simulated 1024×1024 pixel 2^8 phase-level SLM. Target amplitudes are given by the Mandrill test image and target phases are given by the Peppers test image as shown in Fig. 4.

$$G \underset{\mathcal{F}^{-1}}{\overset{\mathcal{F}}{\rightleftarrows}} T, \quad H \underset{\mathcal{F}^{-1}}{\overset{\mathcal{F}}{\rightleftarrows}} R. \tag{5}$$

These definitions can be used with Parseval's theorem to obtain a new expression for the MSE metric.

$$\begin{aligned} E_{\mathrm{MSE}} &= \frac{1}{N_x N_y} \sum_{u=0}^{N_x-1} \sum_{v=0}^{N_y-1} |T_{u,v} - R_{u,v}|^2 \\ &= \frac{1}{N_x N_y} \sum_{x=0}^{N_x-1} \sum_{y=0}^{N_y-1} (T_{u,v} - R_{u,v})(\overline{T_{u,v}} - \overline{R_{u,v}}) \\ &= \frac{1}{N_x N_y} \sum_{x=0}^{N_x-1} \sum_{y=0}^{N_y-1} (G_{x,y} - H_{x,y})(\overline{G_{x,y}} - \overline{H_{x,y}}) \\ &= \frac{1}{N_x N_y} \sum_{x=0}^{N_x-1} \sum_{y=0}^{N_y-1} |G_{x,y} - H_{x,y}|^2. \end{aligned} \tag{6}$$

The key innovation of this paper is to observe that this allows us to determine the value of E_{MSE} on the diffraction field side of the transform from $G_{x,y}$ and $H_{x,y}$, and that this avoids the need for repeatedly projecting changes to the replay fields side to calculate the MSE. If we know the original MSE, then the effect of any change can be determined in $O(1)$ rather than the $O(N_x N_y)$ time required for a calculation on the replay field side.

Result 1. MSE calculation for any phase-sensitive Fraunhofer hologram can be done in the diffraction plane.

3.2 *Linear-Time Holographic Search Algorithm*

Crucially, the calculation of $G_{x,y}$ needs to be done only once—before the hologram calculation commences—in other words, there is no longer a need for repeated Fourier transform evaluations at each iteration. While it may appear obvious that Eq. (4) necessitates that Eqs. (3) and (6) are equivalent, we are unaware of this result having been used previously for hologram generation. Importantly, if we know $E_{\mathrm{MSE}}(G, H)$, changing a single pixel in H at coordinates x, y allows us to write an expression for the new error:

$$\Delta E_{\mathrm{MSE}}(G, H) = |G_{x,y} - H_{x,y} - \Delta H_{x,y}|^2 - |G_{x,y} - H_{x,y}|^2, \tag{7}$$

which runs in constant $O(1)$ time, whereas on the replay side, the update runs in $O(N_x N_y)$ time. This error calculation can be incorporated into the DS algorithm (Fig. 2) to give linear time direct

Mandrill Peppers

Fig. 4 The two test images used.

search (LT-DS). Running the LT-DS algorithm gives the performance graph shown in Fig. 3. Target amplitudes are given by the "Mandrill" test image, and target phases are given by the "Peppers" test image as shown in Fig. 4. With 1024×1024 pixel test images, this gave a $\approx 50{,}000\times$ speed up for the DS algorithm. Similar results are seen for SA. Owing to the amplitude and phase constraint on the target, however, convergent reconstruction quality is extremely poor. This is traditionally solved by using an RoI, a topic we return to in Sec. 4.

It is important to note that, provided the random number generators have the same seed, the hologram given by LT-DS is identical in every way to the hologram provided by DS. The only difference is the Fourier plane on which calculation occurs and the resulting orders of magnitude of speed up. Also worth noting is that we have normalized the values of the hologram here to give a mean of unit energy per pixel on SLM and replay field sides, with a resulting normalization effect on the MSE.

Result 2. The change in MSE of a phase-sensitive hologram due to a single pixel change can be found in constant $O(1)$ time.

3.3 *Effect of Independence*

Section 3.2 used Eq. (7) to reduce the computation required for DS, but maintained the use of the search approach. There are cases, such as when an RoI is taken into account (Sec. 4), where a search approach is necessary, but for the RoI-free case discussed here, we do not actually need to use search syntax at all. Instead, we notice that the effect on the MSE of changing a single pixel is independent of the other pixels. This means that we can actually remove the search element altogether, instead independently assigning values to each individual pixel. This is important as it allows us to parallelize the algorithm for multicore devices. The performance improvement obtained in this way over the sequential version is also shown in Fig. 3 and we have termed it concurrent LT-DS or CLT-DS. The workstation used had an Intel i7-9900K CPU, overclocked to 5.0 GHz with 64 GB of 4000 MHz DDR4 RAM and an RTX 2080TI graphics processing unit (GPU).

Result 3. The change in MSE of a far-field phase-sensitive hologram due to a single pixel change is independent of the effect of other pixels.

3.4 *Realistic Spatial Light Modulator Constraints*

The form of Eq. (6) is a linear minimization problem and is solvable analytically for a range of modulation regimes. This dependency on the properties of the modulator requires us to investigate the case of phase and amplitude modulating devices separately.

3.4.1 *Phase modulating*

If we assume a phase-modulating device where $H_{x,y}$ is confined to the complex circle with magnitude given by the incident illumination $I_{x,y}$, then we can reformat Eq. (7) as

$$\text{minimise} \sum_{x=0}^{N_x-1}\sum_{y=0}^{N_y-1} |G_{x,y} - H_{x,y}|^2 \to \Phi_H = \Phi_G, \tag{8}$$

where Φ_G and Φ_H correspond to the phase vectors of G and H.

Result 4. When aberration and replay field RoIs are neglected, the lowest possible mean square error is achieved for a far-field phase hologram when the phase is equal to the inverse transform of the target replay.

3.4.2 *Amplitude modulating*

If we assume an amplitude modulating device where $H_{x,y}$ is assumed to be confined to $|H_{x,y}| \geq 0$ and $\Phi_H = 0$, then we can reformat Eq. (7) as

$$\text{minimise} \sum_{x=0}^{N_x-1}\sum_{y=0}^{N_y-1} |G_{x,y} - H_{x,y}|^2 \to H = \Re(G). \tag{9}$$

Result 5. When aberration and replay field RoIs are neglected, the lowest possible mean square error is achieved for a far-field amplitude hologram when the SLM amplitude is equal to the real part of the inverse transform of the target replay.

3.5 *Fresnel Holograms, Aberration Correction, and Three Dimensions*

The Fresnel transform used for generating Fresnel holograms is equivalent to the Fourier transform with the addition of a "quadratic phase factor" as in

$$R_{u,v} = \underset{\text{Fresnel}}{\mathcal{F}}\{H_{x,y}\} = \underset{\text{Fourier}}{\mathcal{F}}\{H_{x,y}\Phi_{\text{Fresnel}}\}, \tag{10}$$

where $\Phi_{\text{Fresnel}} = \exp i\pi/\lambda z(x^2 + y^2)$. It can be seen that the Parseval's theorem remains applicable here. Equations (3) and (6) remain equivalent and the results of Secs. 3.4.1 and 3.4.2 remain valid with the addition of an additional phase term.

In fact, for any input phase term dependent only on x and y, we can assert the equivalence of Eqs. (3) and (6). This includes the family of Seidel aberrations.

While we discuss the linear-time algorithm here in the context of 2-D holograms, it is equally applicable to three-dimensional (3-D) holograms generated by means of "Fresnel slices" or the layer-based technique.

4 Incorporating a Region of Interest

The reconstruction quality obtained for complex-valued target fields using the techniques above is often extremely poor, but this is not due to the choice of algorithm. Instead, this is because the problem is overconstrained. One solution that is widely used is to only require a portion of the replay field to match the target image, with the remainder of the replay field being free to take on any value. Mathematically, we can define an RoI mask $M_{u,v}$, where $M_{u,v} = 1$ in the RoI and $M_{u,v} = 0$ otherwise. We then can write MSE as changed error(T, R) to $E_{\text{MSE}}(T, R)$

$$E_{\text{MSE}}(T, R) = \frac{1}{N_x N_y}\sum_{u=0}^{N_x-1}\sum_{v=0}^{N_y-1} M_{u,v}|T_{u,v} - R_{u,v}|^2. \tag{11}$$

Unfortunately, we can no longer use Eq. (4) in order to move this to the SLM side, as Parseval's theorem only holds true if all of space is considered instead of only a subregion of space.

We present here an alternative technique for incorporating an RoI into a linear-time algorithm. We can rewrite Eq. (11) to give the following:

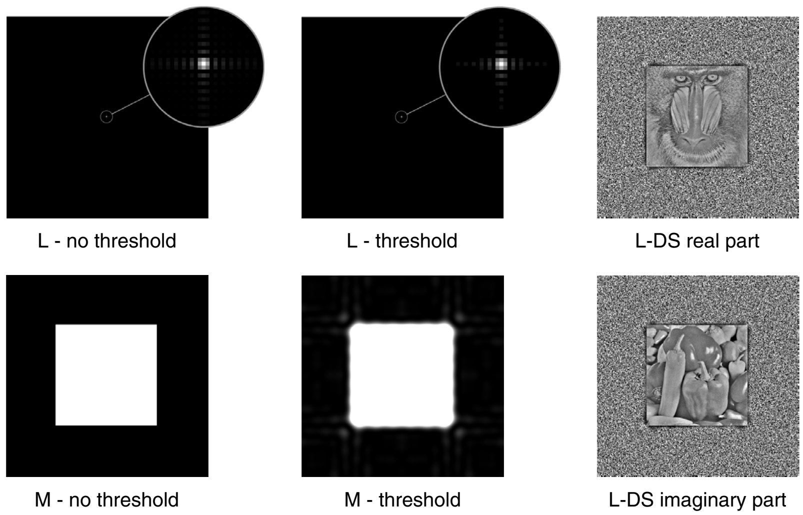

Fig. 5 Mask and inverse transform of mask (left) without thresholding and (center) with thresholding. (Right) Reconstruction of real and imaginary parts for LT-DS. Target amplitudes are given by the Mandrill test image and target phases are given by the Peppers test image as shown in Fig. 4.

$$\begin{aligned}
E_{\mathrm{MSE}} &= \frac{1}{N_x N_y} \sum_{u=0}^{N_x-1} \sum_{v=0}^{N_y-1} |M_{u,v} T_{u,v} - M_{u,v} R_{u,v}|^2 \\
&= \frac{1}{N_x N_y} \sum_{u=0}^{N_x-1} \sum_{v=0}^{N_y-1} M_{u,v} T_{u,v} \overline{M_{u,v} T_{u,v}} - M_{u,v} T_{u,v} \overline{M_{u,v} R_{u,v}} \\
&\quad - \overline{M_{u,v} T_{u,v}} M_{u,v} R_{u,v} + M_{u,v} R_{u,v} \overline{M_{u,v} R_{u,v}} \\
&= \frac{1}{N_x N_y} \sum_{x=0}^{N_x-1} \sum_{y=0}^{N_y-1} F_{x,y} \overline{F_{x,y}} - F_{x,y} \overline{(L * H)_{x,y}} \\
&\quad - \overline{F_{x,y}} (L * H)_{x,y} + (L * H)_{x,y} \overline{(L * H)_{x,y}} \\
&= \frac{1}{N_x N_y} \sum_{x=0}^{N_x-1} \sum_{y=0}^{N_y-1} F_{x,y} \overline{F_{x,y}} - F_{x,y} \overline{K_{x,y}} - \overline{F_{x,y}} K_{x,y} + K_{x,y} \overline{K_{x,y}}, \qquad (12)
\end{aligned}$$

where "*" denotes convolution, "·" denotes the Hadamard or "dot" product and changed "where * denotes convolution and" to "'*' denotes convolution, '·' denotes the Hadamard or 'dot' product and"

$$L \underset{\mathcal{F}^{-1}}{\overset{\mathcal{F}}{\rightleftarrows}} M, \quad F \underset{\mathcal{F}^{-1}}{\overset{\mathcal{F}}{\rightleftarrows}} M \cdot T, \quad K \underset{\mathcal{F}^{-1}}{\overset{\mathcal{F}}{\rightleftarrows}} M \cdot R.$$

Here, $F_{x,y}$ behaves similarly to our previous study and single pixel updates can be determined in $O(1)$. The $K_{x,y}$ corresponds to a convolution though and cannot be evaluated as easily. Fortunately, while convolution is an $O(N_x^2 N_y^2)$ problem, changing a single pixel of a convolution can be somewhat optimized. The convolution term of Eq. (6) is given for any pixel x', y' as

$$K_{x',y'} = \sum_{a=0}^{N_x-1} \sum_{b=0}^{N_y-1} L_{a,b} H_{x'-a,y'-b}. \qquad (13)$$

Recognizing that L is only nonzero for a handful of pixels, this can be calculated in $O(n)$, where n is the number of pixels where $L \neq 0$. The updated equation is given as

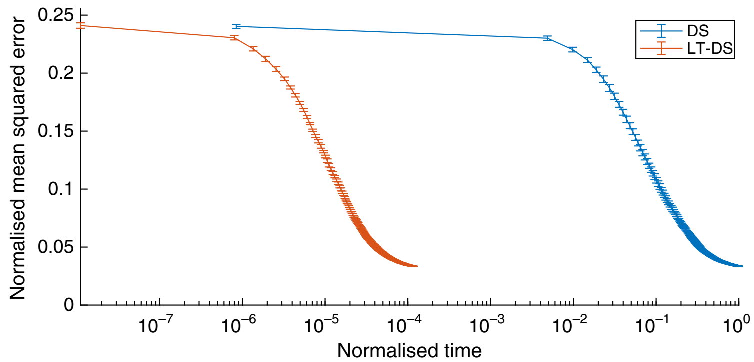

Fig. 6 Performance of DS and linear time DS for a simulated 1024×1024 pixel 2^8 phase-level SLM with mask region thresholded at 45 points. Target amplitudes are given by the Mandrill test image and target phases are given by the Peppers test image as shown in Fig. 4.

$$K_{x',y'} = \sum_{L \neq 0} L_{a,b} H_{x'-a,y'-b}. \tag{14}$$

A change in a single pixel x, y of value $\Delta H_{x,y}$ then causes a difference to the convolution at pixel x', y' as

$$\Delta K_{x',y'} = L_{x'-x,y'-y} \Delta H_{x,y}. \tag{15}$$

Incorporating this back into the MSE equation, the following update step can then be defined.

$$\Delta E_{\mathrm{MSE}} = \frac{1}{N_x N_y} \sum_{x'=0}^{N_x-1} F_{x,y} \overline{\Delta K_{x,y}} - \overline{F_{x,y}} \Delta K_{x,y} + \Delta K_{x,y} \overline{K_{x,y}} + K_{x,y} \overline{\Delta K_{x,y}} + \Delta K_{x,y} \overline{\Delta K_{x,y}}. \tag{16}$$

This can be incorporated into the DS algorithm shown in Fig. 2. Any given mask, $M_{u,v}$ can be given to an arbitrary degree of accuracy by $\mathcal{F}\{L\}$, though, in practice, if L is nonzero for more than a few points, we recommend a change of mask or an alternative approach.

To demonstrate this in action we take the case of L being nonzero only at a selected 45 points out of a 512×512 image. This leads to a mask function similar to Fig. 5 with associated figures. We updated Fig. 5 to include spy glasses

The quality of the mask in Fig. 5 depends on the thresholding value chosen. For many simple masks, over 90% of the power in the mask can be captured by only a few points in L. This corresponds to a slight reweighting of MSE priorities due to differences in value of M.

The performance scales linearly with the number of points in L. For the images in Fig. 5 with L thresholded to 45 points, we see the performance shown in Fig. 6 with identical normalization to that in Fig. 3. The speed improvement when compared to Fig. 3 is lower, however, due to higher number of calculations per iteration, but is still 10,000× faster than the traditional DS approach.

As in Sec. 3.2, the hologram generated using this approach is identical to generating a hologram using DS with mask function M, provided the same random number generator seeds are used in both cases.

5 Further Work

The work described so far is applicable in the case where both the phase and the amplitude of the replay field are to be controlled. The progress made prompts the obvious question of whether this linear-time technique can be applied to phase-insensitive holograms where the error is given as

$$E_{\mathrm{MSE},pi} = \frac{1}{N_x N_y} \sum_{u=0}^{N_x-1} \sum_{v=0}^{N_y-1} [|T_{u,v}| - |R_{u,v}|]^2. \tag{17}$$

Clearly this problem is nonlinear so a best possible solution is improbable. The authors believe, however, that the techniques of this paper should allow a similar movement of an error metric to the SLM side, but have so far been unable to implement this.

6 Conclusions

This paper has presented a new approach to generating holograms for 2-D phase-sensitive replay fields. The discussed algorithm relies on a judicious use of the Parseval's theorem, allowing the phase-sensitive MSE error metric to be calculated from the field in the SLM plane. This allows search algorithms such as SA and DS to run without the need for repeated Fourier transforms, providing a significant acceleration in execution time. Whereas one iteration of a more traditional DS algorithm has a computational cost of $O(N_x N_y)$, iterations of the new proposed implementation have a computation cost as low as $O(1)$. This performance boost is particularly marked for high-definition holograms. For example, with the Tokyo 2020 Olympics being shown in 8k (7680×4320) resolution, the expected performance improvement is over 1 million times faster. The algorithm has been presented for Fraunhofer holograms but has been shown to be equally valid for Fresnel holograms. Conclusions have been drawn for common modulation schemes. An equivalent approach for a phase-insensitive MSE error metric has not been found, but it is felt that further work can address this.

Acknowledgments

The authors would like to thank the Engineering and Physical Sciences Research Council (Grants No. EP/L016567/1, No. EP/T008369/1, No. EP/L015455/1, and No. EP/L015455/1) for its financial support during the period of this research. The authors declare no conflicts of interest.

References

1. D. Gabor, "A new microscopic principle," *Nature* **161**, 777–778 (1948).
2. E. N. Leith and J. Upatnieks, "Reconstructed wavefronts and communication theory," *J. Opt. Soc. Am.* **52**(10), 1123–1130 (1962).
3. A. Maimone, A. Georgiou, and J. S. Kollin, "Holographic near-eye displays for virtual and augmented reality," *ACM Trans. Graphics* **36**(4), 1–16 (2017).
4. T. Widjanarko et al., "Clearing key barriers to mass adoption of augmented reality with computer-generated holography," *Proc. SPIE* **11310**, 113100B (2020).
5. J. Svoboda et al., "Holographic 3-D imaging—methods and applications," *J. Phys. Conf. Ser.* **415**, 012051 (2013).
6. S. C.-Y. Yuen, G. Yaoyuneyong, and E. Johnson, "Augmented reality: an overview and five directions for AR in education," *J. Educ. Technol. Dev. Exchange* **4**(1), 11 (2011).
7. K. Lee, "Augmented reality in education and training," *TechTrends* **56**(2), 13–21 (2012).
8. P. Pessaux et al., "Towards cybernetic surgery: robotic and augmented reality-assisted liver segmentectomy," *Langenbeck's Arch. Surg.* **400**(3), 381–385 (2015).
9. A. Y. Nee et al., "Augmented reality applications in design and manufacturing," *CIRP Ann.* **61**(2), 657–679 (2012).
10. M. Campbell et al., "Fabrication of photonic crystals for the visible spectrum by holographic lithography," *Nature* **404**(6773), 53–56 (2000).
11. J. Grieve et al., "Hands-on with optical tweezers: a multitouch interface for holographic optical trapping," *Opt. Express* **17**(5), 3595–3602 (2009).
12. P. J. Christopher et al., "Improving performance of single-pass real-time holographic projection," *Opt. Commun.* **457**, 124666 (2020).
13. P. J. Christopher et al., "Sympathetic quantization—a new approach to hologram quantisation," *Opt. Commun.* **473**, 125883 (2020).
14. M. Clark and R. Smith, "A direct-search method for the computer design of holograms," *Opt. Commun.* **124**(1), 150–164 (1996).

15. B. K. Jennison, J. P. Allebach, and D. W. Sweeney, "Direct binary search computer-generated holograms: an accelerated design technique and measurement of wavefront quality," *Proc. SPIE* **1052**, 2–9 (1989).
16. B. K. Jennison, J. P. Allebach, and D. W. Sweeney, "Iterative approaches to computer-generated holography," *Opt. Eng.* **28**(6), 629–637 (1989).
17. J.-P. Liu, C.-Q. Yu, and P. W. M. Tsang, "Enhanced direct binary search algorithm for binary computer-generated Fresnel holograms," *Appl. Opt.* **58**, 3735–3741 (2019).
18. M. A. Seldowitz, J. P. Allebach, and D. W. Sweeney, "Synthesis of digital holograms by direct binary search," *Appl. Opt.* **26**, 2788–2798 (1987).
19. J.-H. Kang et al., "Non-iterative direct binary search algorithm for fast generation of binary holograms," *Opt. Lasers Eng.* **122**, 312–318 (2019).
20. J. A. Carpenter and T. D. Wilkinson, "Graphics processing unit-accelerated holography by simulated annealing," *Opt. Eng.* **49**(9), 095801 (2010).
21. S. Kirkpatrick, C. D. Gelatt, and M. P. Vecchi, "Optimization by simulated annealing," *Science* **220**(4598), 671–680 (1983).
22. A. G. Kirk and T. J. Hall, "Design of binary computer generated holograms by simulated annealing: coding density and reconstruction error," *Opt. Commun.* **94**(6), 491–496 (1992).
23. M. P. Dames et al., "Efficient optical elements to generate intensity weighted spot arrays: design and fabrication," *Appl. Opt.* **30**, 2685–2691 (1991).
24. H.-J. Yang, J.-S. Cho, and Y.-H. Won, "Reduction of reconstruction errors in Kinoform CGHS by modified simulated annealing algorithm," *J. Opt. Soc. Korea* **13**, 92–97 (2009).
25. P. J. Christopher, Y. Wang, and T. D. Wilkinson, "Predictive search algorithm for phase holography," *J. Opt. Soc. Am. A* **36**, 2068–2075 (2019).
26. P. J. Christopher et al., "Holographic predictive search: extending the scope," *Opt. Commun.* **467**, 125701 (2020).
27. P. J. Christopher et al., "Improving holographic search algorithms using sorted pixel selection," *J. Opt. Soc. Am. A* **36**, 1456–1462 (2019).
28. P. J. Christopher and T. D. Wilkinson, "Relative limitations of increasing the number of modulation levels in computer generated holography," *Opt. Commun.* **462**, 125353 (2020).

Biographies of the authors are not available.